Flow and transport in the vadose zone: On the impact of partial saturation and Peclet number on non-Fickian, pre-asymptotic dispersion

Emma Ollivier-Triquet, Benjamin Braconnier, Véronique Gervais-Couplet, Souhail Youssef, Laurent Talon, Daniela Bauer

Flow and transport in the vadose zone: On the impact of partial saturation and Peclet number on non-Fickian, pre-asymptotic dispersion

Emma Ollivier-Triquet[a,b], Benjamin Braconnier[a], Véronique Gervais-Couplet[a], Souhail Youssef[a], Laurent Talon[b,*], Daniela Bauer[a]

[a] *IFP Energies Nouvelles, 1 & 4 Av. Bois Préau, 92852 Rueil Malmaison, France*
[b] *Université Paris-Saclay, CNRS, FAST, 91405, Orsay, France.*

Abstract

Transport phenomena in unsaturated porous media still present an important research topic. In particular, in the context of recent environmental concerns, further understanding of contaminant transport in the partially saturated vadose zone is necessary. However, there is currently a lack of understanding of the relationship between water saturation, in particular the two-phase distribution, and dispersion. This is due to the intricate interactions between the two-phase flow and the porous structure, as well as the complexity of the experimental techniques, which prevents a significant number of configurations from being analysed.

We explore passive tracer transport in two-dimensional unsaturated porous media via experimental and numerical methods. To this goal, we conduct co-injection experiments to produce two-phase distributions (air/water) at different saturations in a transparent micromodel that mimics the topology of the Bentheimer sandstone. From these experiments, we generate images using multi-scale multiple-point statistics modeling (MPS). Employing the Lattice Boltzmann method, we calculate velocity and concentration fields for both experimental and generated images under saturated and unsaturated conditions. Our results show strong similarities in velocity distributions, good agreement in concentration profiles, and a matching of dispersion characteristics between experimental and MPS-generated images. MPS enables us to create a variety of unsaturated porous media structures with different topologies but similar transport properties. From these images, we analyse transport over a large range of saturations and Peclet numbers. We observe pre-asymptotic non-Fickian transport regimes characterised by a variance increasing with time according to a power law with exponent $\alpha > 1$. We find that α increases as saturation decreases, due to enhanced flow heterogeneity, and with higher Peclet numbers. This behavior is confirmed through large-scale simulations.

Keywords: Anomalous transport, Dispersion, Unsaturated porous media, Lattice Boltzmann

*Correspondings authors: talon@fast.u-psud.fr

Nomenclature

ϕ	Porosity
θ	Water content
S_w	Water saturation
τ	Tortuosity
k	Permeability
k_r	Relative permeability
L_x	Length of the micromodel
L_y	Width of the micromodel
L_z	Depth of the micromodel
Pe	Peclet number
ν	Fluid kinematic viscosity
ρ	Fluid density
P	Pressure
$\boldsymbol{u}$	Local velocity field
σ_u	Normalized standard deviation of the velocity field

1. Introduction

Human activity influences largely the subsurface, and particularly the unsaturated vadose zone. This part of Earth located below the land surface and just above the water tables is most of the time only partially saturated with water. It plays a key role in hydrogeology, as the refilling of aquifers usually takes place in this part of the subsurface. The vadose zone can be impacted by pollution, coming from agriculture or industrial activities, which impairs the water resources. Furthermore, the water saturation level may vary, notably during periods of droughts or heavy rainfall. Therefore, it is crucial to be able to predict contaminant transport for various saturation conditions in the vadose zone. In contrast to unsaturated media, transport in heterogeneous, saturated porous media has been the subject of numerous studies, e.g reviewed in [1, 2]. However, dispersion in unsaturated porous media still remains a significant research topic, notably because of the complex multiphase flow interactions with the porous structure, which are not yet fully understood.

The difficulty lies in the fact that the volume of pores accessible to pollutants depends on the interaction of the non-miscible air/water flow with the porous medium. Indeed, the presence of air clusters induces a greater flow heterogeneity. As a result, the velocity field presents stagnant zones with very low velocities as well as preferential paths with high velocities [3, 4, 5]. Flow, and consequently transport, will thus depend on both the saturation and the medium heterogeneity. In stagnant zones, transport is controlled by diffusion and is, therefore, very slow. Transport in the preferential paths, however, is mainly advective and much faster, leading to extreme solute displacements [6]. As a result, dispersion in unsaturated porous media is far more complex than in saturated ones. Further comprehension

on the joint influence of the pore topology and the two-phase non-miscible air/water distribution on the macroscopic transport is crucial to fully understand dispersion phenomena in the unsaturated subsurface.

A large number of experiments have been performed to determine the dispersion coefficient or the dispersivity in porous structures at various saturations. However, authors have different points of view on the influence of saturation on dispersion. Many authors note an increase of dispersion/dispersivity in unsaturated porous media, compared to saturated conditions (e.g. [7, 8, 9, 10]), related to an increase in heterogeneity. In contrast, other works highlight non monotonic relations between the saturation and the dispersivity, or the dispersion coefficient [11, 12, 13]. Few other articles show different tendencies from those mentioned above (e.g. [14, 15]). These discrepancies could be explained by the limited number of experiments, which leads to statistical incoherence; and by the different experimental approaches and different ways of interpreting the data.

The determination of a constant dispersion coefficient also assumes that transport is Fickian, i.e. governed by a advection-diffusion equation (ADE). It is worth mentioning that Fickian regime is very frequently observed. Indeed, the central limit theorem states that transport becomes Fickian in an asymptotic regime if the variance of the displacement is finite. However, it has been shown that a Fickian transport model often fails to predict dispersion in unsaturated porous media [7, 16, 17, 18, 6, 19]. A key feature of Fickian transport is the linear growth of the second moment of the concentration field over time. Thus, the most convenient way to determine the Fickian nature of the transport is to analyse the time evolution of the second moment. Often non-Fickian behaviour is characterised by a power law time evolution of this moment, referred to as 'anomalous' dispersion [20, 16, 17, 21]. The main objective of this paper is therefore to assess and quantify the nature of transport in unsaturated porous media by analysing the temporal evolution of the second spatial moment.

The effect of saturation on dispersion has been the subject of numerous studies. In particular, three-dimensional column experiments are often used to study dispersion in unsaturated sand, rock or soil samples (e.g. [8, 10, 11, 9, 7]). In such configurations, due to the opacity of the samples, transport is often analysed using breakthrough curves (average concentration at the outlet). Dispersion in unsaturated porous media can also be studied by means of transparent micromodels. Indeed, micromodels allow direct visualization of the solid structure, two-phase distribution and concentration pattern. Dispersion is then determined from the spatial moments of the concentration profiles as well as the breakthrough curves [7, 6, 5, 4].

The first step in assessing the influence of saturation on the dispersion is to understand the spatial distribution of the immiscible phases. A simple way to generate realistic unsaturated porous media is to co-inject the two immiscible phases. Immiscible multiphase flow processes have been extensively studied using micromodel experiments (e.g. [22, 23, 24, 25, 26**?**]). Multiphase configurations mainly depend on the capillary number, on the saturation of each phase and on the flow history [24]. Many tracer experiments have been performed in micromodels in either saturated (e.g. [27, 28, 29]) or unsaturated (e.g. [30, 31, 12, 6, 5, 4, 32]) conditions. However, transport experiments in micromodels are limited by several aspects.

As dispersion tends to increase in unsaturated conditions, the micromodel size may not always be appropriate. Furthermore, as saturation decreases with flow rate, it is difficult to investigate a wide range of Peclet numbers (ratio of advection time to diffusion time) for a given saturation. In addition, as discussed in [5, 33], it is difficult to experimentally obtain neat tracer injection conditions due to the dispersion in the inlet tubing. Consequently, the experimental uncertainties compromise the analysis of the nature of dispersion.

To overcome these difficulties, several authors have used numerical simulations. The critical factor for these simulations is to ensure an accurate representation of the immiscible phase distribution. Images can be obtained either experimentally or numerically (from two-phase flow simulations or machine learning methods) [34, 4, 19, 17]. The main disadvantage of numerical simulations is the high computational cost of solving the two-phase flow equations.

However, numerical simulations allow a more accurate resolution of the transport equation with a neat inlet condition, a wider range of Peclet number and are less limited in size than experiments. Highly parallelizable Lattice Boltzmann simulations are commonly used to simulate flow and transport in complex porous media [35, 36, 37].

Further understanding of the coupling between pore structure, immiscible phase distribution and transport requires a statistically relevant amount of data. Indeed, as the saturation decreases, heterogeneity becomes more important, as the air cluster size distribution widens.

To address this augmented heterogeneity, one can either increase the sample size or the number of configurations with identical statistical properties. Jiménez-Martinez *et al.* [4] considered a machine learning approach based on multiple-point statistical simulations (MPS) [38] to generate two-phase distributions in a given two-dimensional porous structure consisting of irregularly arranged spheres. The MPS approach, initially developed for geological modeling, makes it possible to generate images with complex features that are derived from a reference image, referred to as the Training Image (TI) and representing the expected structure. In this work, we extend the machine learning approach considered by Jiménez-Martinez *et al.*. However, unlike Jiménez-Martinez *et al.* who only generate the air-water distribution for a given solid configuration, we use an MPS algorithm to generate both different solid and water/air configurations. The training images represent two fluid-phase distributions (air/water) in porous media obtained experimentally, when a steady state is reached and air clusters are immobile. By this approach, the coupling between saturation and pore topology can be easily studied for different structures. Moreover, this method allows a significant statistical analysis.

The article is structured as follows: we begin by presenting experiments on two-phase flow in a micromodel that represents a 2D natural rock formation. These experiments enable the acquisition of a training image database for different phase configurations. In the following section, we introduce the MPS algorithm used to generate the image database with various configurations and different saturations. Then, we will introduce the Lattice Boltzmann simulations performed to solve flow and transport in these images. Finally, we analyse the distribution of air and water in the porous medium as well as the dispersion, Fickian or non-Fickian, depending on the saturation and Peclet number.

2. Experimental and numerical methods

In the following, we briefly present the experimental and numerical methods developed and their validation. Further details can be found in the Supplementary Information.

2.1. Multiphase flow in a micromodel

This section provides an overview of the experiment conducted in an irregular porous glass micromodel to obtain air/water distributions at different saturations. To this end, we apply co-injection of air and water. We performed experiments at various fractional flow rates in order to obtain images at different saturations. We hereby present the micromodel structure and the experimental setup.

2.1.1. Experimental setup

Micromodel. We use a glass micromodel with an inner etched irregular network. The dimensions of the micromodel are $L_y = 10mm$ wide by $L_x = 17mm$ long. The model is wet-etched with depth of $L_z = 40\mu m$. The interior model network is based on an image of a 2D slice of Bentheimer sandstone rock, obtained from X-Ray tomography. It was modified to ensure percolation in 2D leading to a final porosity higher than the one of the original rock. The micromodel is presented in Fig. 1a. The porous medium is characterised by a total number of 2600 grains. The average porosity of the micromodel is $\phi = 66$ % and the permeability including inlet and oulet tubings is 4.7 Darcy (taken from [39]). The micromodel can be considered as strongly water wetting as it is made of glass.

Microfluidic set-up. The micromodel is connected to a Vinduum pump (delivering a continuous flow rate) at lateral inlets for water injection and to a Harvard syringe pump at the center inlet for gas injection. The outlet is connected to the pressure and flow rate sensors. The gas used is ambient air and the liquid is MilliQ water. We used Parker Quink ink as tracer. The value of the diffusion coefficient at our experimental conditions is around $2.710^{-8}mm^2.s^{-1}$ following the measurement of [40]. The micromodel is inserted in a holder and placed horizontally on the optical bench (avoiding gravity effects), above a flat dome red light with adjustable intensity. A high speed camera with a lens is placed above the system to visualize the air-water distributions. The camera JAI (SP-12000M-CXP4 model) provides a 12-megapixel monochrome resolution (4096×3072 pixel), the full-field framerate is 189 frames per second (fps). The acquisition is performed by the Hiris software. The experimental setup is presented in Fig. 1b. The pressure drop of the water phase is measured to determine the permeability of the system. The room temperature was regulated at $21°C$.

Co-injection experiments. The objective of the experimental part is to obtain a homogeneous distribution of trapped air clusters in the micromodel at different water saturations. To this goal, we chose to inject air and water simultaneously in the micromodel at different fractional flow rates, resulting in uniform distributions of the air and the water phase in the micromodel. Modifying the fractional flow rate between air and water results in different water saturations at steady state. The flow rates were in the range of $0.1\mu L.min^{-1}$ and $1mL.min^{-1}$. Co-injection is not maintained over a long period of time but is stopped

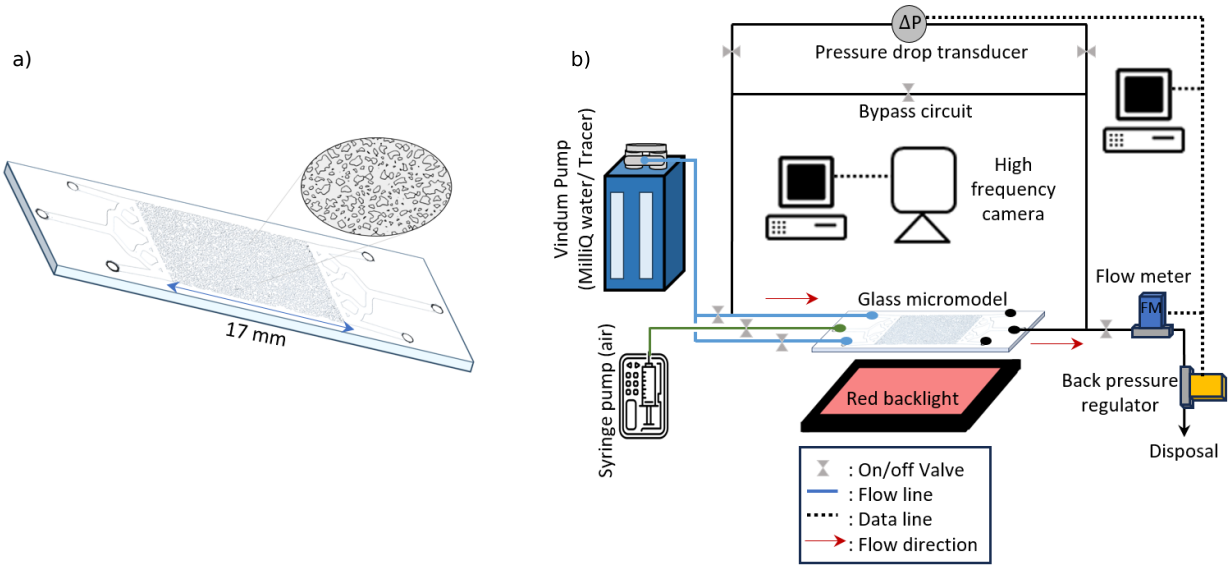

Figure 1: a) Micromodel, b) Experimental setup

once the air distribution reaches a steady state after several seconds. Then we preform the transport experiment. Please note that similar experimental protocols were used for example in [23, 24, 41, 42] providing a deeper analysis of the two-phase distribution resulting from a co-injection procedure.

Image processing. The solid, air and water phases are distinguished through segmentation of the images using a thresholding technique. Each phase is then associated to a specific grey level. Fig. 2 shows the original two-phase distribution in the micromodel a) and the segmented image b). Further details on the image segmentation can be found in the Supplemental Information (SI). The segmented image is analysed using the ImageJ Analyse Particles tool to obtain structure properties: grain and air cluster size as well as shape characteristics. Pore size distribution is computed using ImageJ plugin for Watershed separation on the binarized porous structure.

2.1.2. Characterization of non-Fickian dispersion with spatial moments

Fractional dispersion has been introduced to describe anomalous dispersion where the spatial and/or temporal moments vary according to a power law (e.g. [43, 44]). For example, it can be associated with random walk models such as the Levy walk and Levy flights, which are characterised by broad distributions of temporal or spatial random steps [45, 46, 47].

To characterise non-Fickian dispersion, we determine the temporal evolution of the second spatial moment (see Supplemental Information). We then fit the second moment with a power law with exponent α and a fractional dispersion coefficient D_α^{frac}:

$$\sigma_{fit}^2 = D_\alpha^{frac} t^\alpha. \tag{1}$$

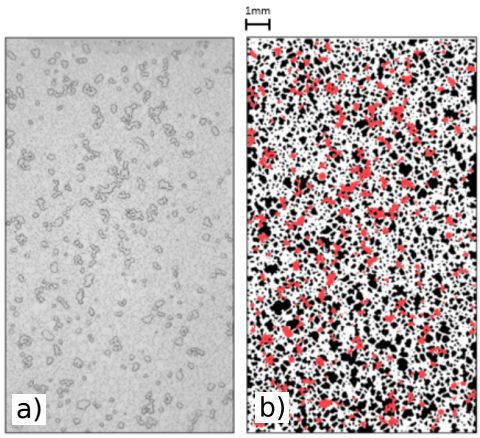

Figure 2: Phase segmentation: a) Raw experimental image with air clusters and water. b) Processed image after phase segmentation, air (red), solid (black), water (white).

The coefficient α characterises the nature of dispersion. If α is close to 1, dispersion is Fickian, it is non-Fickian otherwise. D_α^{frac} quantifies the magnitude of the dispersion (Fickian or not). However, it is worth noting that comparing different values of D_α^{frac} is meaningless as soon as α is different. For this reason, when comparing the evolution of D_α^{frac} for different parameters (Peclet number Pe, S), we are led to impose α.

2.2. Flow and transport equations

We treat the non-wetting phase as immobile because we assume that the flow rate for the tracer experiment is small enough not to displace the gas. Considering higher flow rates would require the use of a two-phase flow solver, which has a much higher computational cost. Consequently, we treat the gas as solid and consider flow and transport only in the water phase. In the following, we first detail the flow and transport equations solved in order to obtain the velocity and concentration field for each configuration. We then briefly present the numerical method used for the resolution of the equations. Finally, we present a comparison between experimental and numerical data.

Flow equation. The local velocity field $\boldsymbol{u}$ in the fluid phase is computed by solving the Darcy-Brinkman equation [48]:

$$-\frac{\rho\nu}{k}\boldsymbol{u} - \boldsymbol{\nabla} P + \rho\nu\nabla^2\boldsymbol{u} = \boldsymbol{0}, \tag{2}$$

where ρ is the density of the fluid, ν represents the kinematic viscosity and P is the pressure.

The Darcy-Brinkman equation is used to compute the depth-average velocity. This allows to describe a 3D velocity field with a 2D equation as demonstrated by [49]. The permeability k can be computed from the depth as $k = {L_z}^2/12$. Physically, the Laplacian term models the transverse diffusion of momentum. It can be used, for example, to describe the boundary layer introduced by the no-slip condition at the wall. In principle, the viscosity in front of the Laplacian should be slightly different from that in the Darcy term [49]. However, in

our case the permeability is so low that the boundary layer is very small and therefore has almost no effect on the dispersion [50, 51]. For simplicity, we have chosen to assume that the two viscosities are equal. And for the same reason, we assume a no-slip condition at the air-water interface.

Advection-Diffusion-Equation. Transport is simulated by solving the local advection-diffusion equation given by

$$\frac{\partial c}{\partial t} + \boldsymbol{u} \cdot \boldsymbol{\nabla} c - D_m \Delta c = 0, \tag{3}$$

where c is the solute concentration in the fluid, $\boldsymbol{u}$ the local velocity vector obtained from the resolution of the Darcy-Brinkman equation and D_m the molecular diffusion coefficient. Similar to previous work, [4], we use a constant diffusion coefficient here. We note however that because the flow profile is not homogeneous in the depth, one should expect that the local flow velocity increases the local dispersion coefficient (Taylor dispersion). By neglecting this effect, we thus assume that the molecular diffusion is dominant over advection at the scale of the gap depth (see also [51]). Indeed, the Peclet number defined with the depth is lower than the one defined using the pore diameter.

Lattice Boltzmann simulations. Two-Relaxation-Time Lattice (TRT) Boltzmann simulations were used to solve Eq. (2) and Eq. (3) to obtain the flow and concentration field in the porous structures. Details on Lattice Boltzmann schemes for the resolution of Eqs. (2) and (3) and the applied boundary conditions are provided in the Supplemental Information file or can be found in [52, 53]. Parameters chosen for the simulation can also be found in the Supplemental Information file. LB computations were performed by adapting the open framework software Walberla [54, 55].

2.3. Comparison of experiments and simulations

We consider continuous tracer injection starting at a specific time $t = 0$, where molecules are injected at the inlet. Fig. 3 shows an image of the micromodel with the three phases (water, air, solid), the porous structure on which simulations are performed (supposing that the gas behaves as the solid), the velocity field in the fluid phase and the concentration field.

We evaluate the influence of these simulation assumptions on transport and the suitability of the method for studying transport in unsaturated micromodels. This is achieved by performing a comparative analysis between the experimental work and Lattice Boltzmann simulations for three different saturations as shown in Fig. 4. Since the numerical and experimental injection conditions are not the same, the comparison requires to shift the origin of time and position. Notably, as the front is more dispersed in the experiments, a position relative to the real position in the experimental case is defined with an offset subtracted to compensate for the spreading at the inlet. Qualitative agreement is then observed, in particular the preferential paths and stagnant, dead end zones are fairly well reproduced. To be more quantitative, we plot the experimental and numerical concentration profiles (see Fig. 5a-c) at different time. As can be seen, there is an agreement between

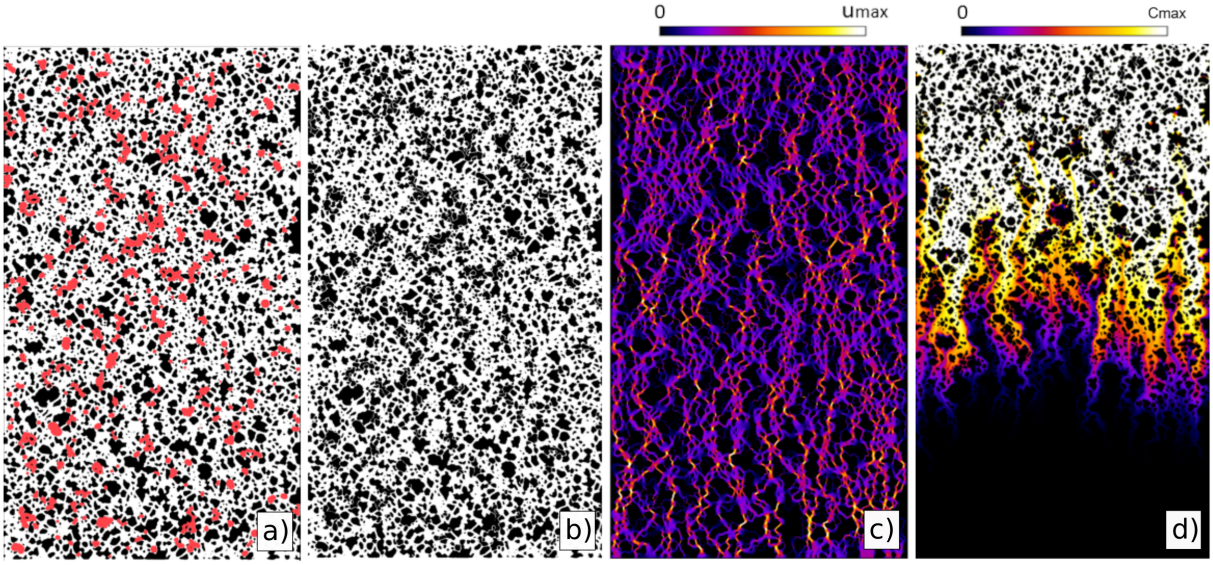

Figure 3: a) Segmented image, air (red), solid (black), water (white). b) Binary image with air clusters as solid (black) used for the velocity field simulation. c) Velocity field magnitude. d) Concentration field with continuous injection from the top.

the two profiles that persists over time. This agreement is then confirmed by comparing the time evolution of the second moment of the profiles in Fig. 5d. However, there is a difference at long times for low saturations. This is due to the high degree of heterogeneity within the system, that is reflected in the concentration profile. It is important to acknowledge that this heterogeneity represents the main challenge in understanding transport in unsaturated porous media. Consequently, the system might not be inherently representative, as the size of the micromodel may be insufficient to achieve a smooth enough signal. As mentioned in the introduction, one way to overcome this difficulty consists in generating a large number of different synthetic but realistic porous media with the adequate characteristics to capture the transport behavior. We propose here to investigate the use of the MPS algorithm to generate such images. Another way consists in increasing the size of the system, which is unfortunately more time consuming.

2.4. Generation of unsaturated, artificial porous media: multiple-point statistics modeling (MPS)

In order to generate unsaturated, artificial porous media having the same structural and statistical properties as the experimental ones, we apply here the multi-scale MPS algorithm described in [56, 57, 58, 59] to the experimental images. MPS algorithms allow to generate images with complex shapes and structures. Their leading idea consists in retrieving information about the desired shape, spatial distribution and connection of the objects from a training image (TI), that represents a model of the expected structure. This information is then used to fill iteratively the simulation grid, resulting in a synthetic medium with a spatial distribution based on the previous characteristics. Further details on the multi-scale MPS algorithm used in this work can be found in the Supplemental Information.

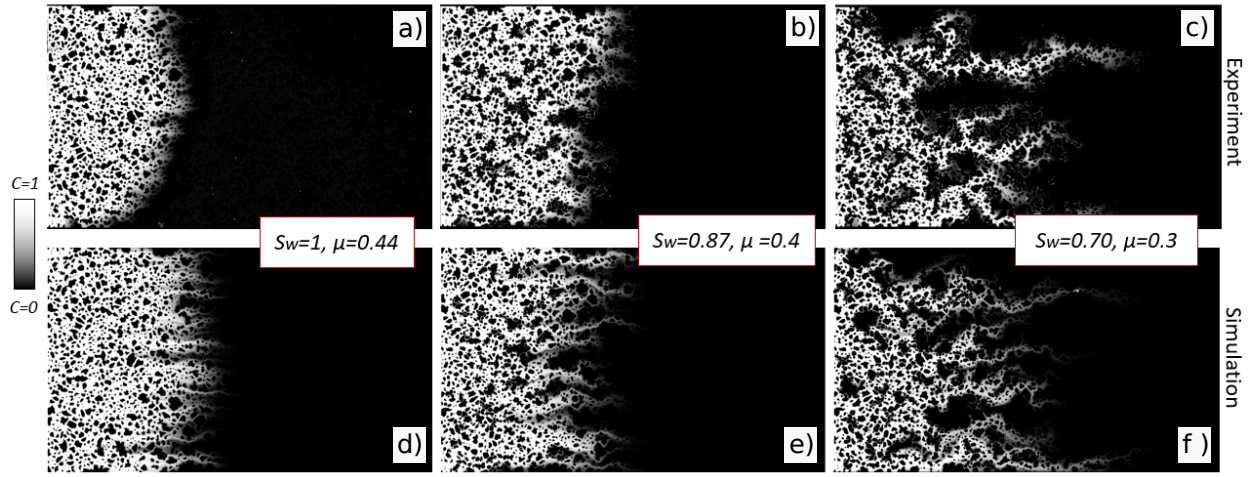

Figure 4: Comparison of experimental and simulated concentration fields at the same mean position of the front μ (first moment of the concentration profile) for three saturation values. μ is normalized by the medium length L_x. $C = 1$ corresponds to $C = C/C_{max}$

The MPS algorithm is applied here with training images derived from experiments and consisting of two-fluid-phase distributions (air/water) in porous media. The training images considered here are not the experimental images, but cleaned versions of these images obtained by removing non-physical artefacts resulting from the image processing, such as some air clusters completely enveloping grains or water contained in grains. Elements of small size whose effect on the flow is negligible are also suppressed. As detailed in the Supplementary Information, the MPS algorithm parameters are chosen as a trade-off between the simulation time and the quality of the results. The generated images present small defects that are not physical: discontinuities of the different phases, absence of water meniscus between grains and air clusters, inclusions in grains or air clusters. These defects may be lessen with other configuration parameters for the MPS algorithm, but at the cost of longer simulation times. Instead, we apply here a post-processing algorithm to the generated images to suppress these defects (see Supplemental Information).

2.4.1. Validation of the MPS algorithm method for flow and transport in MPS generated images

The quality of the resulting generated images was assessed on three different saturation values ($S_w = 1, S_w = 0.87$ and $S_w = 0.70$). We conducted a comparison of various structural characteristics between the experimental and the MPS generated images. These characteristics include the distribution of pores and throats, as well as the size distribution of air clusters. The MPS algorithm proved to be effective in accurately replicating the structural properties of unsaturated porous media as discussed in the Supplemental Information. In addition, we compared flow and transport properties of the generated structures and the experimental ones. To this goal, we simulated the velocity and concentration fields using

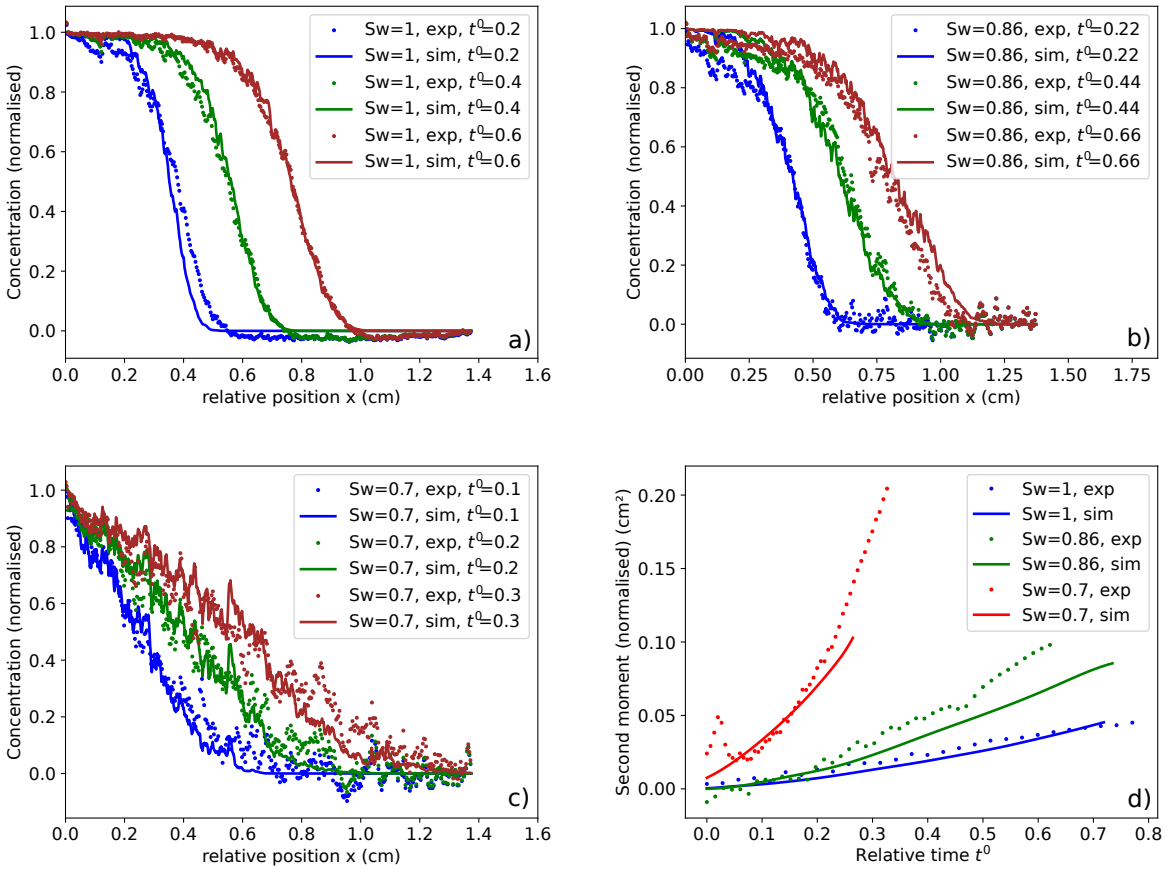

Figure 5: a-c) Comparison of experimental and simulated concentration profiles for the same air/solid configuration and three saturation values ($S_w = 1$, $S_w = 0.86$ and $S_w = 70$) at three normalized times. d) Comparison of the second moment evolution with the normalised time t' for the three saturations. An offset has been subtracted to the second moment for a better comparison of the slopes.

the Lattice Boltzmann method (LBM) described above. As presented in the Supplemental Information, the velocity fields show a very good agreement.

Furthermore, Fig. 6 shows the concentration fields in the experimental and generated images for three saturations. The patterns of dispersion, such as the preferential flow paths and the stagnant dead end zones, are correctly reproduced for the three saturations. Also, the transport properties, characterised by the concentration profiles and the second moment of the dispersion, showed a very good agreement as well (see Supplemental Information file).

In summary, the dispersion behaviour showed consistency between the generated and experimental porous media over all investigated saturation levels. The methodology presented in this study provides a valuable means of investigating dispersion in unsaturated porous media over a wide range of saturations, including different phase configurations and porous media sizes.

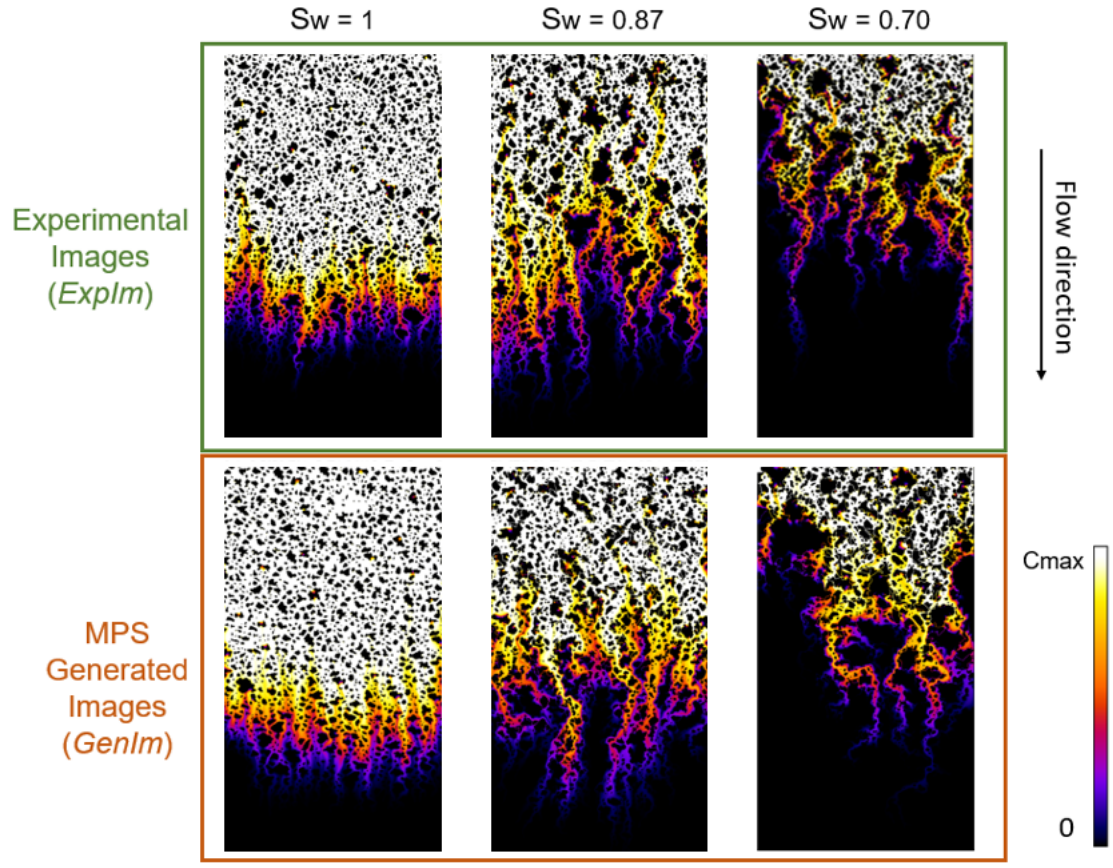

Figure 6: Assessment of the MPS method to study flow and transport. The flow and transport have been simulated using LBM with the original experimental images and the MPS generated images. Simulated concentration fields are given for three saturation values at $t = 1.2 \cdot 10^5$ LB units, $C_{\max} = 1$.

3. Numerical results

3.1. Image datasets

By conducting multiphase flow experiments, we obtained phase distributions from co-injection, covering a saturation range from 0.55 to 1. Our dataset resulting from experiments consists of 25 images. From this dataset, we extracted sub-images, called "training images" (TI) to generate new realizations. Using a sufficiently large number of training images, we can create a training image dataset that covers the various phase configurations present in the micromodel and takes into account their inherent variability.

As explained above, two different approaches are employed to deal with the heterogeneity of the unsaturated porous media. We can either analyse a large number of small generated images, or we can analyse one single, larger image. This results in two different sets of data:

- The "small size" dataset: This dataset comprises images that are approximately equivalent in size to the micromodel ($L_y{}^* = 1980$ pixels, $L_x{}^* = 3780$ pixels or $L_y = 0.90$

cm, $L_x = 1.73$ cm). To capture the system's variability, we generate multiple realizations from each training image. This dataset enables us to study short-term dispersion phenomena within a computationally feasible time-frame.

- The "large size" dataset: the images within this dataset are approximately four times longer ($L_y{}^* = 1980$ pixels, $L_x{}^* = 18000$ pixels, or $L_y = 0.90$ cm and $L_x = 8.3$ cm). However, due to their larger dimensions, simulating flow and transport in these images involves significantly higher computational costs (9000 processors were used in this case, compared to 180 for the shorter images). Therefore, only a limited number of these longer images was used.

3.2. Influence of water saturation on flow properties (small size dataset)

In this section, we investigate the influence of saturation on the flow properties, such as permeability, tortuosity and velocity distribution which are computed from the velocity fields (see Fig. 7).

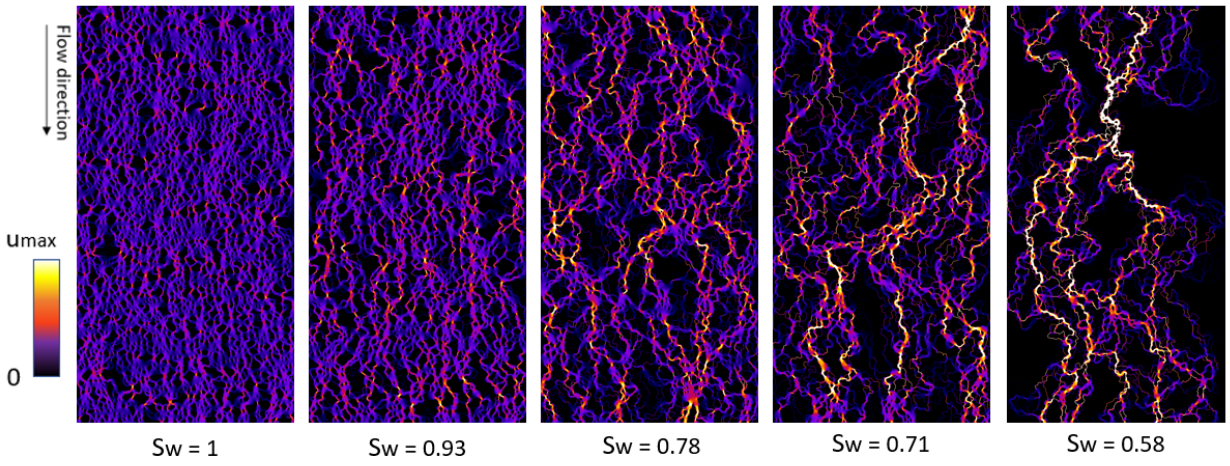

Figure 7: Norm of the velocity fields normalized by the mean flow rate for different saturations (MPS generated images). u_{max} is different for every case.

3.2.1. Permeability

Considering the fact that many permeability models incorporate the water content as a parameter, we define $\theta = \phi S_w$ to allow comparisons, where $\phi = 0.66$ is constant.

Fig. 8a illustrates the evolution of the effective permeability $kk_r(S_w)$, where k_r is the relative permeability corresponding to the water content θ. kk_r increases as the water content, or saturation, increases. In the fully saturated medium ($S_w = 1$, $\theta = \phi = 0.66$), the permeability equals 20 Darcy. As the saturation decreases to its minimal value ($S_w = 0.55$ and $\theta = 0.40$), the relative permeability tends to zero. Please note, that in this case, the effective permeability of the fully saturated micromodel is much higher than values provided

in the Experimental setup. This is due to the fact, that inlet and outlet tubings included in the experimental acquisition of the permeability reduce the latter.

Numerous experimental and numerical studies have extensively explored the relationship between porosity, water content and permeability in saturated and unsaturated media (see for instance [60, 61]). Many of them propose a power law relationship with the porosity or the saturation (e.g. [62, 63]). Because the effective permeability tends to zero for a non zero value of water content, we fit our data using the following relation: $kk_r = R(\theta - \theta_0)^c$, with $R = 153$, $c = 2.2$, and $\theta_0 = 0.3$. And thus

$$kk_r(S_w) = R\phi^c(S_w - S_0)^c, \tag{4}$$

with $S_0 = \theta_0/\phi$.

In summary, the evolution of the effective permeability of the medium is consistent with certain classical models that establish the relationship between permeability and porosity in experimental systems. Consequently, the effective permeability kk_r of the generated images can be modelled by empirical laws with physical parameters.

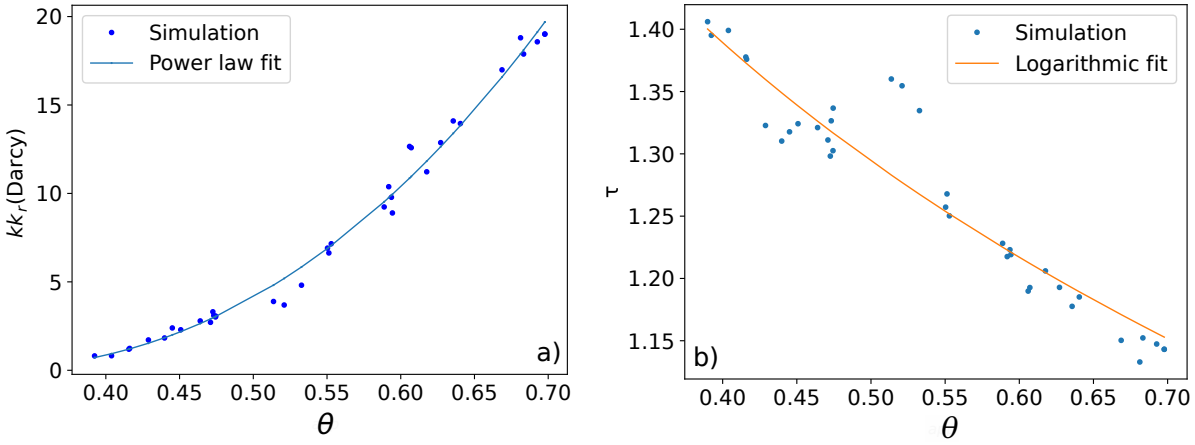

Figure 8: a) Effective permeability kk_r as a function of the water content $\theta = \phi S_w$. The continuous line corresponds to the following power law fit: $kk_r = R(\theta - \theta_0)^c$, with $(R, c, \theta_0) = (159.3, 2.3, 0.3)$. b) Tortuosity τ as a function of the water content θ. The continuous line is a logarithmic fit: $\tau = 1 - p \ln \theta$, with $p = 0.43$.

3.2.2. Tortuosity

Tortuosity quantifies the complexity of the flow paths within the porous material. A simple approach to calculate tortuosity is as follows: $\tau = \frac{\langle |\mathbf{u}| \rangle}{\langle |u_x| \rangle}$, where $|\mathbf{u}|$ is the velocity norm and $\langle |u_x| \rangle$ is the average streamwise velocity component.

In Fig. 8b we show that tortuosity decreases with increasing saturation, suggesting that flow paths become more tortuous at low saturations, which can be observed from the velocity fields shown in Fig. 7. At lower saturations (or water content) the tortuosity reaches a value of 1.4, indicating that the transverse and longitudinal velocities are of the same order of magnitude. Here again, there is a lack of consistency in models that incorporate the connection between tortuosity and saturation. However, numerous models exist to explain

the relationship between tortuosity and porosity (see [64] for more information), among them logarithmic models as for example proposed by [65]. We applied this logarithmic model to fit our data:

$$\tau = 1 - p \ln \theta, \tag{5}$$

with $p = 0.43$.

In summary, the evolution of flow tortuosity aligns with classical models that describe the relationship between tortuosity and porosity in experimental model systems. We remind that we include the gas in the definition of porosity (water content).

3.2.3. Flow velocity distribution

In Fig. 9a, the distribution of normalized velocity, $|\mathbf{u}|/\langle|\mathbf{u}|\rangle$, is plotted for various saturation values. It is observed that as the saturation decreases, the velocity distribution becomes wider, and the tail of the distribution extends towards lower velocities. This widening suggests the formation and expansion of dead-end regions within the medium. Notably, at lower saturation levels, a second peak emerges at very low velocities ($|\mathbf{u}|/\langle|\mathbf{u}|\rangle \sim 10^{-5}$), indicating the presence of nearly stagnant zones in the flow. Additionally, there is a spreading towards high velocities with increasing saturation, especially below $S_w = 0.70$. These high velocities arise from the formation of preferential paths with high velocity. This flow heterogeneity can be quantified using the velocity standard deviation σ_u. Fig. 9b reveals that the standard deviation decreases as the saturation increases. For the lowest saturation values, the standard deviation is approximately three times higher than that in saturated conditions. The velocity standard deviation can be reasonably fitted with a power law:

$$\sigma_u \simeq a S_w^c + b \tag{6}$$

with $(a, b, c) = (0.62, 0.02, -1.8)$.

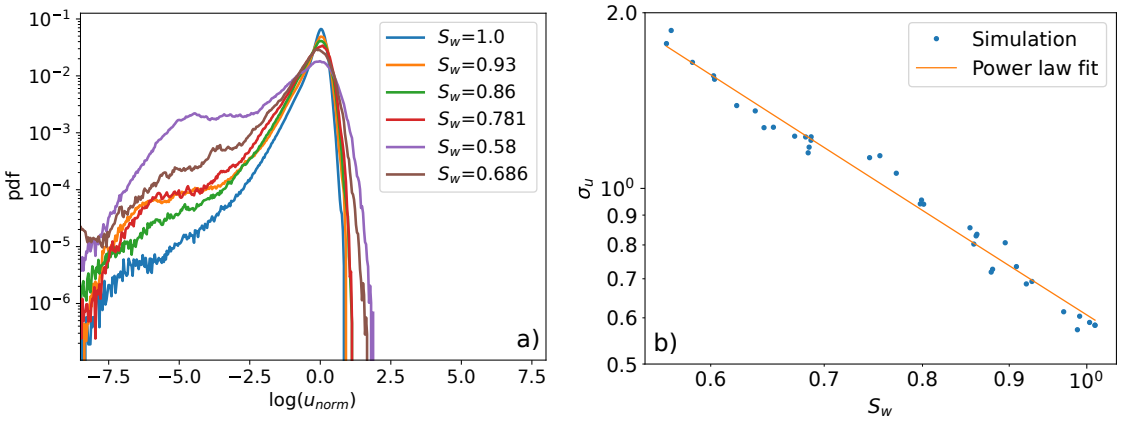

Figure 9: a) For different saturations, distributions of $\log(u_{norm})$, with $u_{norm} = |\mathbf{u}|/\langle|\mathbf{u}|\rangle$, the interstitial velocity magnitude normalized by the mean interstitial velocity. b) Normalized standard deviation of the interstitial velocity as a function of saturation. The line corresponds to a power law fit: $\sigma_u = a S_w^c + b$, with $(a, b, c) = (0.62, 0.02, -1.8)$.

3.3. *Effect of water saturation and Peclet number on transport (small size dataset)*

We perform LBM simulations on MPS generated images, covering the experimental range of saturation $[0.55, 1]$ and explore the following range of Peclet numbers: $Pe \in [0.001, 1000]$, where the Peclet number is defined as

$$Pe = \frac{\langle |\mathbf{u}| \rangle d_{\text{pore}}}{D_m}. \tag{7}$$

$\langle |\mathbf{u}| \rangle$ is the mean local velocity, d_{pore} the mean pore diameter of the porous medium and D_m the molecular diffusion coefficient.

3.3.1. *Effect of saturation on dispersion*

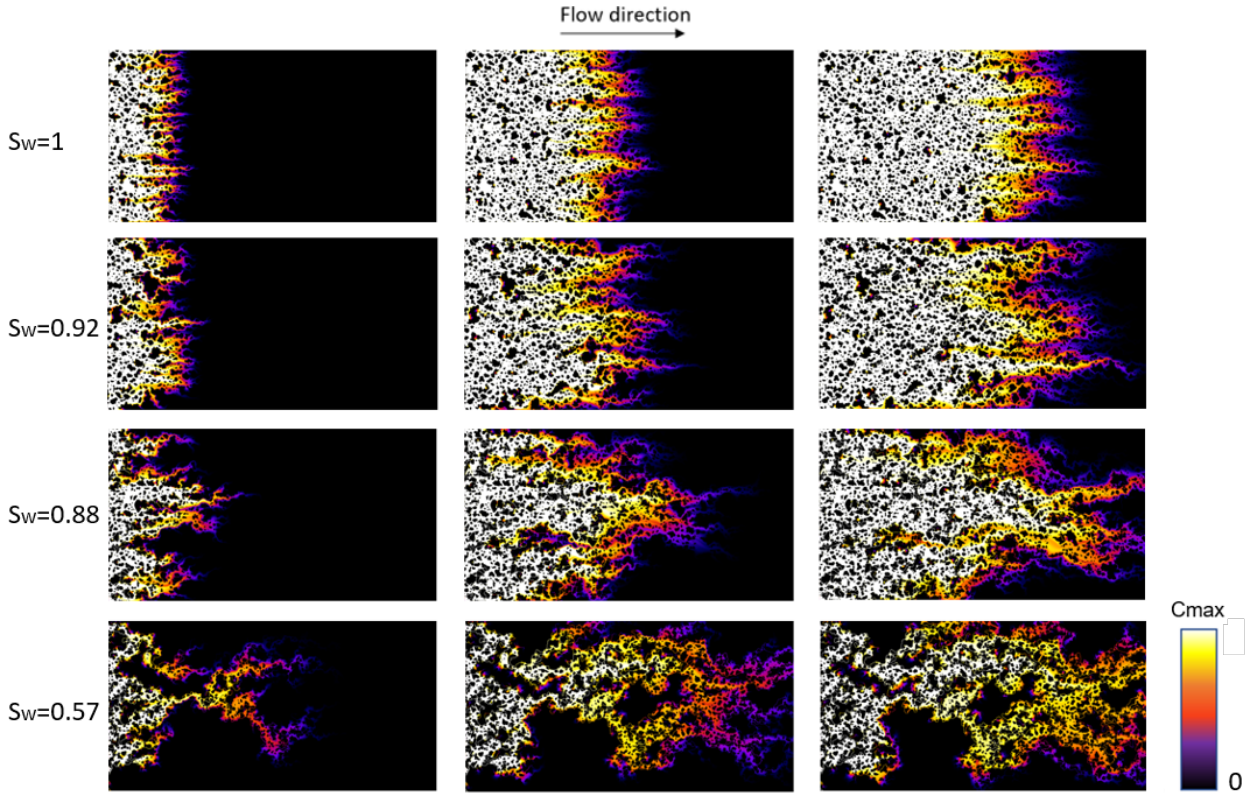

Figure 10: Concentration fields for four saturation values and three mean positions of the concentration front ($\mu_0 = 0.18L_x$, $\mu_1 = 0.43L_x$, $\mu_2 = 0.65L_x$) with $Pe = 100$.

Fig. 10 shows the time evolution of the concentration fields for different saturations and $Pe = 100$. At full saturation the concentration front is relatively flat. As the saturation decreases, the front becomes more heterogeneous and spreads faster with time. In particular, preferential flow paths and dead end zones become more pronounced. We characterise dispersion by the second moment as a function of time, as shown in Fig. 11a. For this Peclet number, we observe that the second moment is not proportional to time, in saturated and unsaturated conditions. The dispersion is therefore non-Fickian for any saturation. To

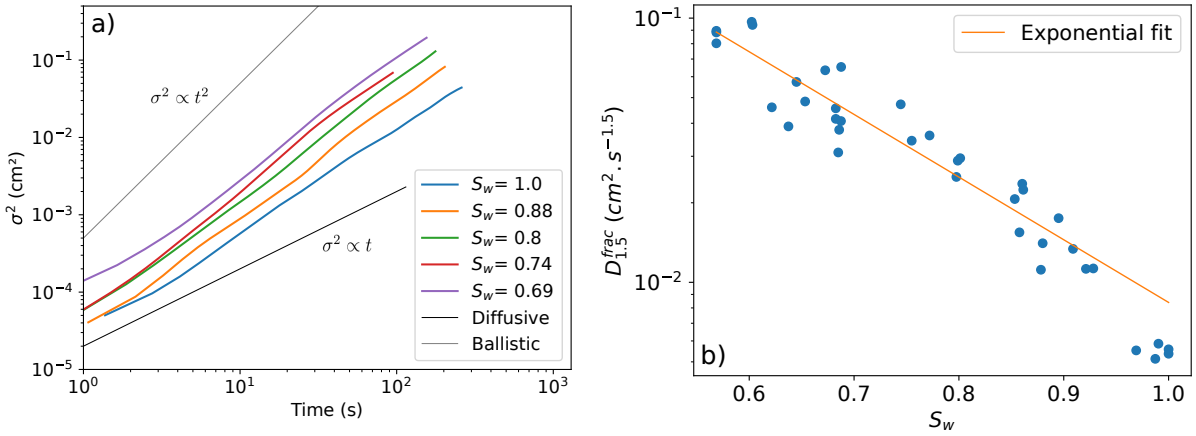

Figure 11: a) Second moment as a function of time for different saturations with $Pe = 100$. b) Fractional dispersion coefficient as a function of saturation. The continuous line represents an exponential trend, $D_{1.5}^{frac} = b \exp^{-S_w a}$, with $(a, b) = (5.5, 2.0)$, diffusive regime: $\sigma^2 \propto t$, ballistic regime: $\sigma^2 \propto t^2$.

quantify the dispersion magnitude, we compute the mean of the power law coefficient α for all the realizations and saturations, which is equal to $\langle \alpha \rangle = 1.5$. We then compute the fractional dispersion coefficient with this exponent using Eq. (1). Results are presented in Fig. 11b. The fractional dispersion coefficient increases by more than a decade as the saturation decreases from $S_w = 1$ to $S_w = 0.55$. Roughly speaking, the decay follows an exponential trend for the unsaturated cases, with a small inflection around $S_w = 1$. This trend is consistent with the observation in 3D porous media by [11, 66], although these authors fit their data with a function different from ours (power law decay).

3.3.2. Effect of the Peclet number on dispersion

In this section, we explore the influence of the Peclet number on dispersion, starting with saturated conditions followed by unsaturated conditions.

Saturated medium. Fig. 12 illustrates how the power law index α evolves with the Peclet number. At high Peclet numbers, α exceeds one (~ 1.4) and decreases as the value of the Peclet number decreases. The exponent reaches 1 for Peclet numbers less than one. In other words, for high Peclet numbers, the dispersion is dominated by advection, leading to non-Fickian behaviour. The non-Fickian character slowly diminishes with decreasing Peclet number as diffusion becomes more effective. When diffusion and advection are of the same order ($Pe \in [1, 10]$), α reaches 1 (Fickian transport). We also compute the pure diffusion case ($Pe = 0$) and observe, as expected, that the transport is Fickian ($\alpha = 1$) and the value of the dispersion is below the molecular diffusion coefficient, allowing to define a diffusive tortuosity $\tau_d = \frac{1}{D^*(Pe=0)} = 2.15$. The effect of Peclet number on dispersion has been thoroughly studied in the literature for saturated porous media [67, 68, 69]. Most of these studies report the evolution of the dispersion coefficient, *i.e* assuming Fickian transport $\alpha = 1$, as a function of the Peclet number. For comparison, we thus compute in Fig. 12 a normalized effective dispersion coefficient, imposing $\alpha_{imposed} = 1$: $D^* = D_{\alpha=1}^{frac}/D_m$. For high

Peclet number values, D^* is approximately proportional to the Peclet number. As the Peclet number decreases, D^* slowly converges to a constant value smaller than 1. This evolution with the Peclet number is thus in good agreement with the literature.

In conclusion, we have shown that while the evolution of the dispersion coefficient with the Peclet number is qualitatively consistent with the literature, the transport deviates from the Fickian one for $Pe \gtrsim 10$. In this range, the value of α rises above 1.

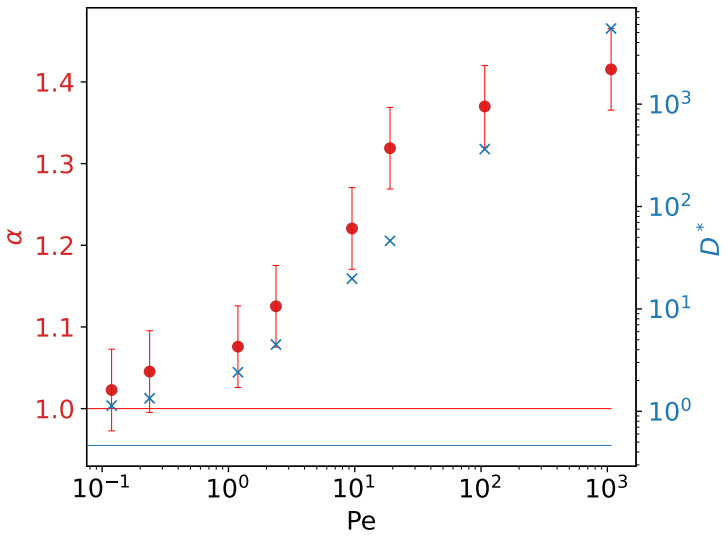

Figure 12: Evolution of the power law index α (dots) and the normalized effective dispersion coefficient $D^* = D^{frac}_{\alpha=1}/D_m$ (crosses) with the Peclet number for the saturated case $S_w = 1$. The values for no flow condition ($Pe = 0$) are shown with a red and blue line for $\alpha(Pe = 0)$ and $D^*(Pe = 0)$ respectively. Error bars of α are estimated from the power law fit.

Unsaturated medium. We now examine the influence of the Peclet number on α and $D^* = D^{frac}_{\alpha=1}/D_m$ for different saturations. Fig. 13a displays how the exponent α changes as the Peclet number varies. For all saturations we observe a similar dependence on the Peclet number as in the saturated case. Namely, there is a transition from Fickian behaviour ($\alpha = 1$) at low Pe to non-Fickian behaviour ($\alpha \sim 1.4$) at higher Peclet number. However, we note that the Peclet number of the transition depends on the saturation, with the transition occurring at lower Pe (almost two decades) for the lowest saturation. Also, for lower saturations, the transition is stiffer. Fig. 13b shows the evolution of the normalised effective dispersion coefficient D^* ($\alpha = 1$) with the Peclet number. Similarly to the saturated case, the dispersion coefficient increases with the Peclet number. As for the saturated case the dispersion coefficient is constant for low Peclet number. At a given Peclet number, D^* starts to increases with the onset of the transition depending on the saturation. For lower saturation, the onset occurs at a significantly lower value of the Peclet number. For a given Peclet number, D^* is therefore higher at lower saturation. Interestingly, the onset of the transition for α and D^* is of the same order of magnitude of Peclet number. Note that the

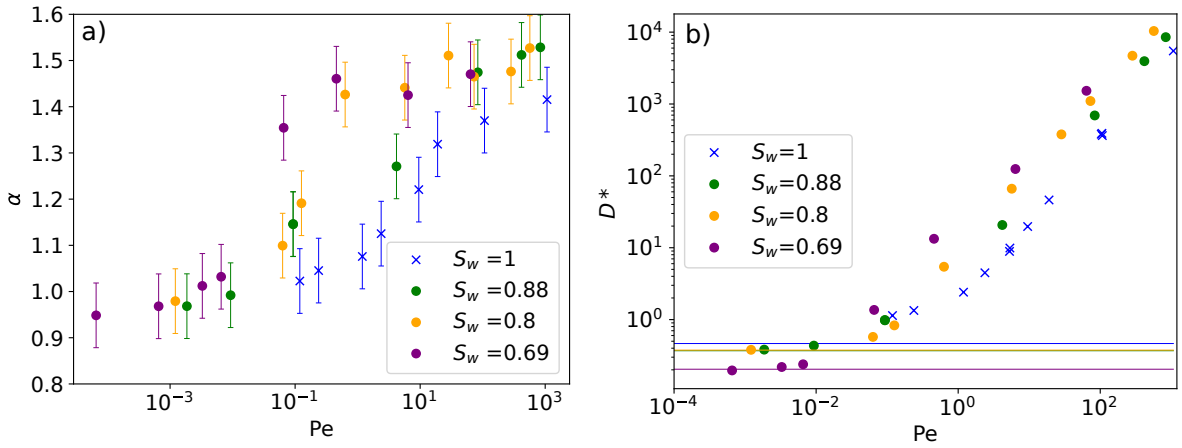

Figure 13: Evolution of the power law index α a) and normalized dispersion coefficient b) with the Peclet number for different saturation values. The values of D^* for no flow condition are shown by horizontal lines. Error bars of α are estimated from the power law fit.

value of D^* in purely diffusive conditions ($Pe = 0$, straight line in Fig. 13) decreases with reducing saturation: the diffusive tortuosity of the medium thus rises with saturation.

Fig. 14 shows the evolution of α with saturation for different, specific Peclet numbers. For high Peclet numbers, α is relatively independent of saturation, but as the Peclet number decreases, the dependency becomes more pronounced. In 2D regular structures, Velasquez et al. [17] observed a transition from Fickian to non-Fickian behavior with decreasing water saturation. 3D transport experiments using NMR imaging in homogeneous rock with various degrees of saturation [70] show non-Fickian dispersion even in saturated conditions, with a non-Fickian character enhanced by lower saturations. Our results are therefore representative of a general tendency and most likely not constraint by the geometry of the porous media. As discussed in the introduction, similar micromodel transport experiments have been performed by [3, 33, 4, 71] using cylindrical pillars of different diameters. Although they observed non-Fickian transport for the unsaturated case, the exponent α is difficult to compare quantitatively. For example, ballistic behaviour ($\alpha = 2$) was observed in [33], whereas in our case α is below 1.5 even at high Peclet number. This difference could be attributed to the porous structure of the micromodel, which strongly influences the immiscible distribution.

To conclude, dispersion is non-Fickian for a larger range of Peclet numbers in unsaturated conditions. At high Peclet number, transport is dominated by advection even in saturated conditions and transport is non-Fickian. For intermediate Peclet number, dispersion is Fickian only for high saturations but not for smaller saturations. For sufficiently low Peclet numbers, dispersion is dominated by diffusion and becomes Fickian even for the lowest saturations.

3.4. Large size dataset simulations

In the previous section, we observed a non-Fickian behavior for a large range of parameters. However, it is worth recalling that asymptotic non-Fickian behavior is only expected

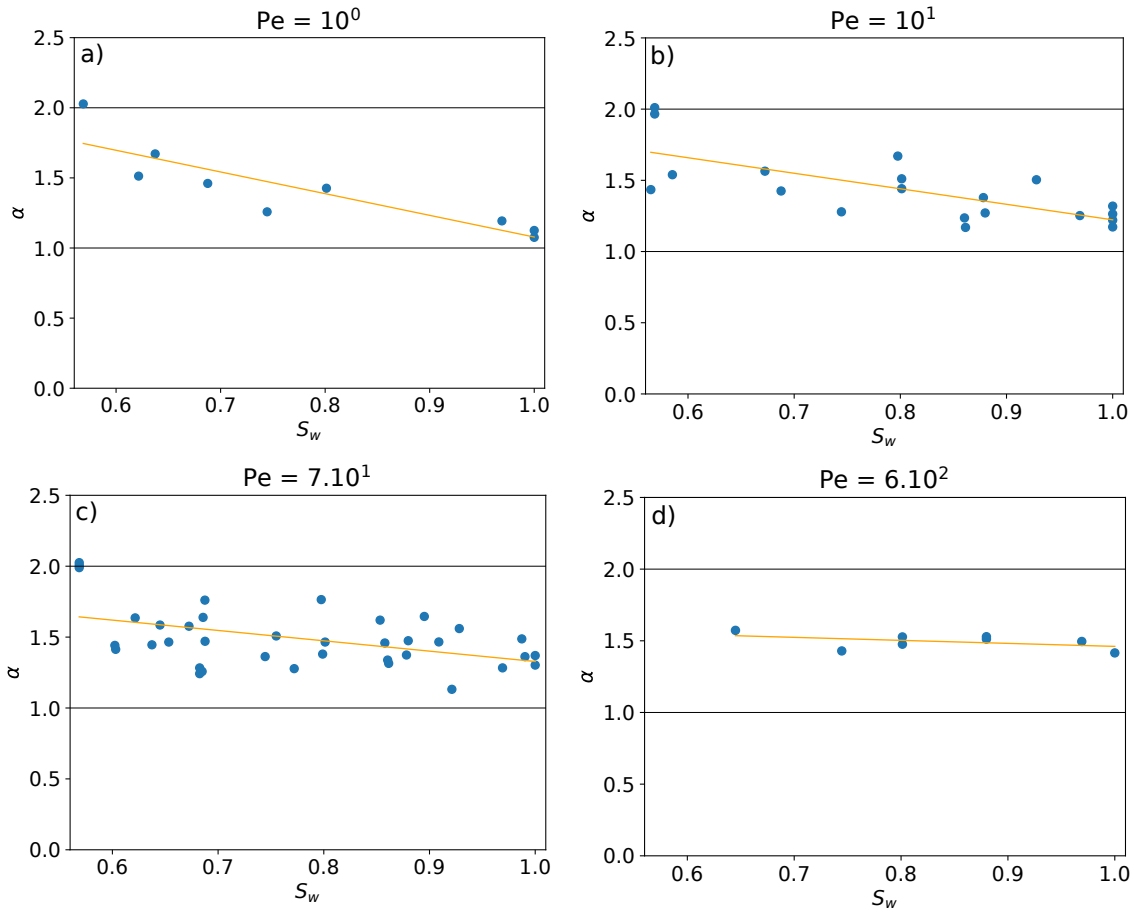

Figure 14: Dependence of the power law index α with saturation for different Peclet numbers. The trend is highlighted by a linear fit to each curve. The blue points correspond to values computed for the short dataset $L_x = 3780$. a) $Pe = 10^0$, $\alpha_{fit} = -0.05S_w + 1.5$ b) $Pe = 10^1$, $\alpha_{fit} = -0.05S_w + 1.5$ c) $Pe = 7 \times 10^1$, $\alpha_{fit} = -1.08S_w + 2.4$ d) $Pe = 6 \times 10^3$, $\alpha_{fit} = -1.7S_w + 2.8$.

for non-finite variance of the velocity distribution. As shown in Fig. 9, the variance of the velocity field increases with decreasing saturation while remaining finite. This means that one should expect the dispersion to be Fickian in an asymptotic regime, suggesting that the observed non-Fickian regime would only be transient. For this reason, we performed several simulations with a very large domain as described above. Fig. 15a shows the variance as function of time for five different saturations with an intermediate Peclet number, $Pe = 5$. The evolution of the variance confirms the non-Fickian tendency over longer times, but no change in the temporal behavior (e.g. transition to the asymptotic regime) was observed for any saturation. We conclude that our domain is still too short to reach an asymptotic regime. However, since the exponents α in the large size domain (Fig. 15b) and the smaller one are similar (α increases with decreasing saturation), it indicates that the small size samples are large enough and more efficient for quantifying the transport properties in partially saturated porous media.

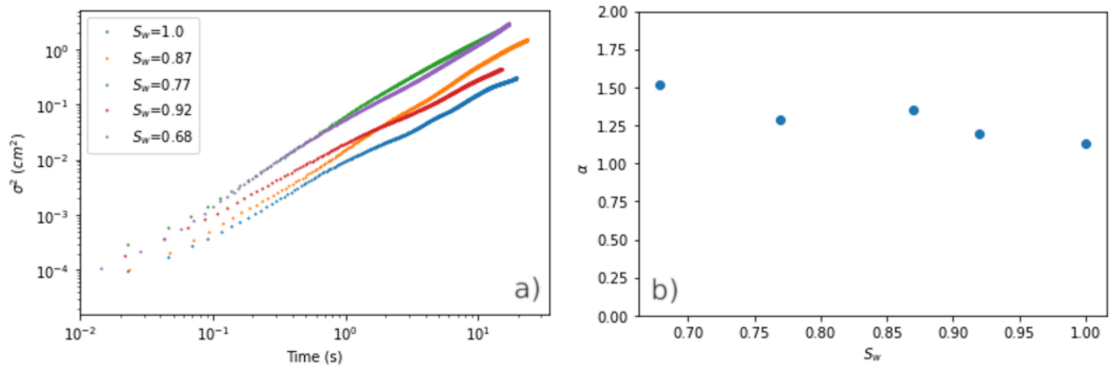

Figure 15: Results for large system size (18000 × 1980 pixels^2) for $Pe = 5$. a) Displacement variance as function of time for different saturations. b) Corresponding power law index α as a function of saturation.

4. Conclusions and Discussion

In this article we investigated passive transport phenomena in two-dimensional unsaturated porous media coupling experiments and numerical simulations. Two-phase distributions (air/water) for different saturations were obtained by means of co-injection experiments in a micromodel reproducing the topology of a Bentheimer sandstone. From these experimental images, we generated new images using a multi-scale MPS algorithm. Using Lattice Boltzmann method, we computed velocity and concentration fields in both experimental and generated images, for saturated and unsaturated conditions. We showed that the velocity distributions were very similar. The concentration profiles were in very good agreement and the variance indicates that the dispersion characteristics of the experimental images are well reproduced by the MPS images. Consequently, MPS allowed the generation of a large number of unsaturated porous media images having a new topology but similar properties.

For a large number of samples covering the saturation range between 0.55 and 1, we computed transport for different Peclet numbers. The main result of this study is the

observation of non-Fickian behaviour for a wide range of these parameters. This behaviour is characterised by a variance that increases with time according to a power law with an exponent α. We have determined the evolution of this exponent as a function of saturation and Peclet number. Overall, α increases with decreasing saturation due to the increase in flow heterogeneity, and increases with the Peclet number. This behavior has been confirmed by large size simulations. However, these large size domain simulations did not exhibit the expected transition to a Fickian regime.

As discussed in the introduction, the physical origin of anomalous transport lies in the strong heterogeneity of velocity field and residence time (see also [71]). It is therefore not surprising to find that decreasing the water saturation enhances anomalous behavior, as it increases both the extent of the velocity distribution, but also the number of stagnant zones. What is more interesting, however, is the fact, that while saturation greatly increases the prefactor of the power law D_*, it changes only slightly the exponent α (around 1.5 at high Peclet number). The exponent seems to depend mainly on the Peclet number: 1 for low values and 1.5 for high values. In fact, diffusion increases the exchange rate between different velocity zones. Reducing the Peclet number therefore decreases the effects of extreme velocity values and thus favours normal transport. However, we observe that decreasing saturation shifts the Peclet number value of the transition by increasing the extent of the high and low velocity zones. We also note, that, while the α exponent in our case becomes relatively constant for high Peclet number, other studies in different geometries show higher exponents [33, 16, 17]. This suggests that the exponent value may depend on the geometry of the porous structure.

There are several ways to extend this study. First of all, it would be worthwhile to repeat this method for 3D geometry. If 3D X-ray tomography allows the determination of air and water distribution in natural media, the main drawback is the small sample size. A 3D MPS algorithm could therefore be used to generate many other configurations to perform statistical analysis on more realistic rock. This would also allow lower saturation values to be investigated. Another possible direction could be to analyse more carefully the origin of the non-Fickian regime. For example, one could use the CTRW framework to determine the resident time distribution. One possible outcome of such approach would be the estimation of the duration of this transient non-Fickian regime.

Acknowledgment

This work was performed using CCRT HPC resource (TOPAZE supercomputer). The authors would like to thank Sarah Bouquet and Guillaume Batôt for using the MPS and LB code respectively.

Supplemental Information

Supplementary material related to this article can be found in the Supplemental Information file. The SI file provides further details on the image processing and the MPS algorithm. It also precises the LBM schemes to solve Darcy-Brinkman and Advection-diffusion equations. Additional results are also illustrated.

References

[1] M. Dentz, T. Le Borgne, A. Englert, B. Bijeljic, Mixing, spreading and reaction in heterogeneous media: A brief review, Journal of contaminant hydrology 120 (2011) 1–17.

[2] M. Dentz, J. J. Hidalgo, D. Lester, Mixing in porous media: concepts and approaches across scales, Transport in Porous Media 146 (1) (2023) 5–53.

[3] J. Jiménez-Martínez, P. d. Anna, H. Tabuteau, R. Turuban, T. L. Borgne, Y. Méheust, Pore-scale mechanisms for the enhancement of mixing in unsaturated porous media and implications for chemical reactions, Geophysical Research Letters 42 (13) (2015) 5316–5324.

[4] J. Jiménez-Martínez, A. Alcolea, J. Straubhaar, P. Renard, Impact of phases distribution on mixing and reactions in unsaturated porous media, Adv Water Resour 144 (2020) 103697. doi:10.1016/j.advwatres.2020.103697.

[5] V. Leontidis, S. Youssef, D. Bauer, New insights into tracer propagation in partially saturated porous media, Oil & Gas Science and Technology – Revue d'IFP Energies nouvelles 75 (2020) 29. doi:10.2516/ogst/2020021.

[6] S. Hasan, V. Joekar-Niasar, N. Karadimitriou, M. Sahimi, Saturation dependence of non-fickian transport in porous media, Water Resour Res 55 (2) (2019) 1153–1166. doi:10.1029/2018wr023554.

[7] M. Bromly, C. Hinz, Non-fickian transport in homogeneous unsaturated repacked sand, Water Resour Res 40 (7). doi:10.1029/2003wr002579.

[8] M. Maraqa, R. Wallace, T. Voice, Effects of degree of water saturation on dispersivity and immobile water in sandy soil columns, J. Contam. Hydrol. 25 (3-4) (1997) 199–218. doi:10.1016/s0169-7722(96)00032-0.

[9] G. Nützmann, S. Maciejewski, K. Joswig, Estimation of water saturation dependence of dispersion in unsaturated porous media: experiments and modelling analysis, Adv Water Resour 25 (5) (2002) 565–576. doi:10.1016/s0309-1708(02)00018-0.

[10] D. Haga, Y. Niibori, T. Chida, Hydrodynamic dispersion and mass transfer in unsaturated flow, Water Resour Res 35 (4) (1999) 1065–1077. doi:10.1029/1998wr900111.

[11] I. Padilla, T.-C. Yeh, M. Conklin, The effect of water content on solute transport in unsaturated porous media, Water Resour Res 35 (11) (1999) 3303–3313. doi:10.1029/1999wr900171.

[12] N. Karadimitriou, V. Joekar-Niasar, M. Babaei, C. A. Shore, Critical role of the immobile zone in non-fickian two-phase transport: A new paradigm, Environmental Science & Technology 50 (8) (2016) 4384–4392. doi:10.1021/acs.est.5b05947.

[13] A. Raoof, H. Nick, S. Hassanizadeh, C. Spiers, Poreflow: A complex pore-network model for simulation of reactive transport in variably saturated porous media, Computers & Geosciences 61 (2013) 160–174.

[14] J. Vanderborght, H. Vereecken, Review of dispersivities for transport modeling in soils, Vadose Zone J 6 (1) (2007) 29–52. doi:10.2136/vzj2006.0096.

[15] J. Birkholzer, C.-F. Tsang, Solute channeling in unsaturated heterogeneous porous media, Water Resour Res 33 (10) (1997) 2221–2238. doi:10.1029/97wr01209.

[16] D. Triadis, F. Jiang, D. Bolster, Anomalous dispersion in pore-scale simulations of two-phase flow, Transport in Porous Media 126 (2) (2018) 337–353. doi:10.1007/s11242-018-1155-6.

[17] A. Velásquez-Parra, T. Aquino, M. Willmann, Y. Méheust, T. L. Borgne, J. Jiménez-Martínez, Sharp transition to strongly anomalous transport in unsaturated porous media, Geophys Res Lett 49 (3).

[18] A. Cortis, B. Berkowitz, Anomalous transport in "classical" soil and sand columns, Soil Science Society of America Journal 68 (5) (2004) 1539–1548. doi:10.2136/sssaj2004.1539.

[19] Z. Dou, X. Zhang, C. Zhuang, Y. Yang, J. Wang, Z. Zhou, Saturation dependence of mass transfer for solute transport through residual unsaturated porous media, International Journal of Heat and Mass Transfer 188 (2022) 122595.

[20] B. Berkowitz, H. Scher, S. E. Silliman, Anomalous transport in laboratory-scale, heterogeneous porous media, Water Resources Research 36 (1) (2000) 149–158. doi:10.1029/1999wr900295.

[21] L. Talon, E. Ollivier-Triquet, M. Dentz, D. Bauer, Transient dispersion regimes in heterogeneous porous media: On the impact of spatial heterogeneity in permeability and exchange kinetics in mobile–immobile transport, Advances in Water Resources 174 (2023) 104425.

[22] D. Zhang, R. Zhang, S. Chen, W. Soll, Pore scale study of flow in porous media: Scale dependency, REV, and statistical REV, Geophys Res Lett 27 (8) (2000) 1195–1198. doi:10.1029/1999gl011101.
[23] K. Tallakstad, H. Knudsen, T. Ramstad, G. Løvoll, K. Måløy, R. Toussaint, E. Flekkøy, Steady-state two-phase flow in porous media: statistics and transport properties, Physical review letters 102 (7) (2009) 074502.
[24] T. Chevalier, D. Salin, L. Talon, A. Yiotis, History effects on nonwetting fluid residuals during desaturation flow through disordered porous media, Phys. Rev. E 91 (4). doi:10.1103/physreve.91.043015.
[25] F. Kazemifar, G. Blois, D. Kyritsis, K. Christensen, A methodology for velocity field measurement in multiphase high-pressure flow of CO_2 and water in micromodels, Water Resour Res 51 (4) (2015) 3017–3029. doi:10.1002/2014wr016787.
[26] N. Haque, A. Singh, U. Saha, Experimental visualization and analysis of multiphase immiscible flow in fractured micromodels using micro-particle image velocimetry, J. Energy Res. Technol. 144 (2). doi:10.1115/1.4050958.
[27] J. Wan, T. Tokunaga, C.-F. Tsang, G. Bodvarsson, Improved glass micromodel methods for studies of flow and transport in fractured porous media, Water Resour Res 32 (7) (1996) 1955–1964.
[28] Y. Corapcioglu, S. Chowdhury, S. Roosevelt, Micromodel visualization and quantification of solute transport in porous media, Water Resour Res 33 (11) (1997) 2547–2558. doi:10.1029/97WR02115.
[29] F. Watson, J. Maes, S. Geiger, E. Mackay, M. Singleton, T. McGravie, T. Anouilh, T. Jobe, S. Zhang, S. Agar, et al., Comparison of flow and transport experiments on 3d printed micromodels with direct numerical simulations, Transp Porous Media 129 (2) (2019) 449–466.
[30] J. Wan, J. Wilson, Colloid transport in unsaturated porous media, Water Resour Res 30 (4) (1994) 857–864. doi:10.1029/93wr03017.
[31] N. K. Karadimitriou, S. M. Hassanizadeh, A review of micromodels and their use in two-phase flow studies, Vadose Zone Journal 11 (3) (2012) vzj2011.0072. doi:10.2136/vzj2011.0072.
[32] N. Karadimitriou, V. Joekar-Niasar, O. Brizuela, Hydro-dynamic solute transport under two-phase flow conditions, Scientific reports 7 (1) (2017) 1–7.
[33] J. Jiménez-Martínez, T. L. Borgne, H. Tabuteau, Y. Méheust, Impact of saturation on dispersion and mixing in porous media: Photobleaching pulse injection experiments and shear-enhanced mixing model, Water Resour Res 53 (2) (2017) 1457–1472. doi:10.1002/2016wr019849.
[34] R. Aziz, V. Joekar-Niasar, P. Martinez-Ferrer, Pore-scale insights into transport and mixing in steady-state two-phase flow in porous media, Int. J. Multiph. Flow 109 (2018) 51–62.
[35] L. Talon, D. Bauer, N. Gland, S. Youssef, H. Auradou, I. Ginzburg, Assessment of the two relaxation time lattice-boltzmann scheme to simulate stokes flow in porous media, Water Resources Research 48 (4).
[36] Z. Zaafouri, G. Batôt, C. Nieto-Draghi, B. Rotenberg, D. Bauer, B. Coasne, Lattice boltzmann method for adsorption under stationary and transient conditions: Interplay between transport and adsorption kinetics in porous media, Physical Review E 104 (1) (2021) 015314.
[37] C. Zhang, K. Zhang, J. Mo, Z. Li, T. Suekane, Y. Wang, M. Li, Pore-scale investigation of solute dispersion behavior in porous media under a two-phase co-flow condition, Advances in Water Resources 186 (2024) 104664.
[38] J. Straubhaar, P. Renard, T. Chugunova, Multiple-point statistics using multi-resolution images, Stochastic Environmental Research and Risk Assessment 34 (2) (2020) 251–273. doi:10.1007/s00477-020-01770-8.
[39] C. Yeates, S. Youssef, E. Lorenceau, Accessing preferential foam flow paths in 2d micromodel using a graph-based 2-parameter model, Transport in Porous Media 133 (2020) 23–48.
[40] S. Lee, H. Lee, I. Lee, C. Tseng, Ink diffusion in water, European journal of physics 25 (2) (2004) 331.
[41] L. Talon, R. Bouguemari, A. Yiotis, D. Salin, Fragmentation and coalescence dynamics of non-wetting blobs during immiscible two-phase flows in porous media, Physical Review Fluids 8 (9) (2023) 093602.
[42] A. Anastasiou, I. Zarikos, A. Yiotis, L. Talon, D. Salin, Steady-state dynamics of ganglia populations during immiscible two-phase flows in porous micromodels: Effects of the capillary number and flow ratio on effective rheology and size distributions, Transport in Porous Media (2024) 1–25.

[43] D. A. Benson, S. W. Wheatcraft, M. M. Meerschaert, Application of a fractional advection-dispersion equation, Water resources research 36 (6) (2000) 1403–1412.
[44] J. H. Cushman, T. R. Ginn, Fractional advection-dispersion equation: A classical mass balance with convolution-fickian flux, Water resources research 36 (12) (2000) 3763–3766.
[45] M. M. Meerschaert, D. A. Benson, B. Bäumer, Multidimensional advection and fractional dispersion, Physical Review E 59 (5) (1999) 5026.
[46] M. M. Meerschaert, D. A. Benson, H.-P. Scheffler, P. Becker-Kern, Governing equations and solutions of anomalous random walk limits, Physical Review E 66 (6) (2002) 060102.
[47] R. Metzler, J. Klafter, The random walk's guide to anomalous diffusion: a fractional dynamics approach, Physics Reports 339 (1) (2000) 1–77. doi:10.1016/S0370-1573(00)00070-3.
[48] H. Brinkman, A calculation of the viscous forces exerted by a flowing fluid on a dense swarm of particles, Appl. Sci. Res. sect A1 (1947) 27–39.
[49] J. Zeng, Y. Yortsos, D. Salin, On the Brinkman correction in unidirectional Hele-Shaw flows, Phys. Fluids 15 (2003) 3829–3836.
[50] N. Jarrige, I. Bou Malham, J. Martin, N. Rakotomalala, D. Salin, L. Talon, Numerical simulations of a buoyant autocatalytic reaction front in tilted hele-shaw cells, Phys. Rev. E: Stat. Phys. Plasmas Fluids Relat. Interdisciplin. Top. 81 (2010) 066311. doi:10.1103/PhysRevE.81.066311.
[51] C. Soulaine, J. Maes, S. Roman, Computational microfluidics for geosciences, Frontiers in Water 3. doi:10.3389/frwa.2021.643714.
[52] I. Ginzburg, G. Silva, L.Talon, Analysis and improvement of Brinkman lattice Boltzmann schemes: Bulk, boundary, interface. similarity and distinctness with finite elements in heterogeneous porous media, Phys. Rev. E: Stat. Phys. Plasmas Fluids Relat. Interdisciplin. Top. 91 (2015) 023307. doi:10.1103/PhysRevE.91.023307.
[53] I. Ginzburg, Truncation errors, exact and heuristic stability analysis of two-relaxation-times lattice boltzmann schemes for anisotropic advection-diffusion equation, Commun. Comput. Phys. 11 (5) (2012) 1439–1502. doi:10.4208/cicp.211210.280611a.
[54] M. Bauer, S. Eibl, C. Godenschwager, N. Kohl, M. Kuron, C. Rettinger, F. Schornbaum, C. Schwarzmeier, D. Thönnes, H. Köstler, et al., walberla: A block-structured high-performance framework for multiphysics simulations, Computers & Mathematics with Applications 81 (2021) 478–501.
[55] C. Godenschwager, F. Schornbaum, M. Bauer, H. Köstler, U. Rüde, A framework for hybrid parallel flow simulations with a trillion cells in complex geometries, in: Proceedings of the International Conference on High Performance Computing, Networking, Storage and Analysis, 2013, pp. 1–12.
[56] C. Gardet, M. LeRavalec, E. Gloaguen, Pattern-based conditional simulation with a raster path: a few techniques to make it more efficient, Stoch Env Res Risk A 30 (2) (2016) 429–446. doi:10.1007/s00477-015-1207-1.
[57] C. Gardet, Modélisation multi-échelles de réservoir et calage d'historique de production, Ph.D. thesis, Université Pierre et marie Curie (2014).
[58] B. Doligez, M. LeRavalec, S. Bouquet, M. Adelinet, A review of three geostatistical techniques for realistic geological reservoir modeling integrating multi-scale data, Bulletin of Canadian Petroleum Geology 63 (4) (2015) 277–286.
[59] C. Gardet, M. LeRavalec, Multiscale multiple point simulation based on texture synthesis, 14th European Conference on the Mathematics of Oil Recovery, ECMOR 2014doi:10.3997/2214-4609.20141871.
[60] J. Bear, Dynamics of Fluids in Porous Media, Elsevier, New York, 1988.
[61] F. A. Dullien, Porous media: fluid transport and pore structure, Academic press, 1991.
[62] R. H. Brooks, Hydraulic properties of porous media, Colorado State University, 1965.
[63] Y. Bernabé, A. Maineult, 11.02 - physics of porous media: Fluid flow through porous media, in: G. Schubert (Ed.), Treatise on Geophysics (Second Edition), second edition Edition, Elsevier, Oxford, 2015, pp. 19–41. doi:10.1016/B978-0-444-53802-4.00188-3.
[64] B. Ghanbarian, A. G. Hunt, R. P. Ewing, M. Sahimi, Tortuosity in porous media: A critical review, Soil Science Society of America Journal 77 (5) (2013) 1461–1477. doi:10.2136/sssaj2012.0435.
[65] A. Koponen, M. Kataja, J. Timonen, Tortuous flow in porous media, Physical Review E 54 (1) (1996)

406–410. doi:10.1103/physreve.54.406.
[66] T. Sato, H. Tanahashi, H. A. Loáiciga, Solute dispersion in a variably saturated sand, Water Resources Research 39 (6).
[67] T. Perkins, O. Johnston, A review of diffusion and dispersion in porous media, Society of Petroleum Engineers Journal 3 (01) (1963) 70–84. doi:10.2118/480-pa.
[68] J. Fried, M. Combarnous, Dispersion in porous media, in: Advances in hydroscience, Vol. 7, Elsevier, 1971, pp. 169–282.
[69] P. Mostaghimi, B. Bijeljic, M. J. Blunt, Simulation of flow and dispersion on pore-space images, in: All Days, SPE, 2010. doi:10.2118/135261-ms.
[70] V. Guillon, M. Fleury, D. Bauer, M.-C. Néel, Superdispersion in homogeneous unsaturated porous media using nmr propagators, Physical Review E 87 (4) (2013) 043007.
[71] I. Ben-Noah, J. J. Hidalgo, J. Jimenez-Martinez, M. Dentz, Solute trapping and the mechanisms of non-fickian transport in partially saturated porous media, Water Resources Research 59 (2) (2023) e2022WR033613.